RESEARCH PAPER

Experimental and Numerical Assessment of the Effect of Transverse, Pointed Aft, and Re-entrant Vee Steps as well as Ventilation on Hydrodynamic Performance of Mono-hull Planing Crafts in Calm Water

Sayyed Mahdi Sajedi[1] · **Parviz Ghadimi[1]** ⓘ

Abstract

Stepped planing hulls have been the focus of many studies over the years. Step in the bottom of a planing vessel can be created in different forms for improving its hydrodynamic performance. In this paper, the performance of three stepped planing models with three different types of steps and a model with no step are compared, experimentally and numerically. The types of steps used in these models are transverse, pointed aft, and re-entrant Vee shapes. These models are tested in a towing tank. Experiments are performed at Froude numbers of 0.21–1.97, and the distance from the center of gravity to the aft of the models is 30% of the overall length of the models. The models are then numerically simulated using Star-CCM + software. Three-dimensional analysis of these models is performed by finite volume method (FVM). Volume of fluid (VOF) model is used to capture the free surface and overset technique is used to provide dynamic mesh. The computed trim, rise-up, and drag are compared with those of experimental models. The numerical results are observed to be in good agreement with experimental measurements. Subsequently, the wetted surface area, pressure contour of the bottom, wave pattern, wake formation behind the models, and keel line pressure are compared among different models. The obtained results indicate that stepped models are all stable longitudinally and have less drag than non-stepped model. The model equipped with pointed aft step exhibits less drag due to proper ventilation, and the model equipped with re-entrant Vee shape step has more resistance than other stepped models.

Keywords Stepped planing hull · Experimental tests · Numerical simulation · Step shape · Wave pattern · Overset technique

1 Introduction

Reducing the resistance and increasing the speed of high-speed craft have always been one of the primary aims of designers in developing new hull forms for this type of vessels. Therefore, they have taken an essential step toward increasing the stability and decreasing the drag of the vessel by introducing different novel hulls. Planning hulls are one of the most common types of high-speed crafts used for variety of military and recreational purposes. The development of various types of longitudinal discontinuities such as spray rails as well as transverse discontinuities such as transverse steps can have a significant effect on reducing the drag and increasing the stability of planing hulls (Niazmand Bilandi et al. 2018). Among the most essential advantages of stepped hulls are the low ratio of drag to lift at high speeds and the decrease in wetted surface area due to the flow separation from the step(s). In fact, the two important dimensions of the step, which are the height of the step and the longitudinal distance of the step from the aft of the vessel, play an important role in the hydrodynamics of the stepped hulls. Transverse steps have so far been designed in various types such as flat, dinaplan, and sweepback. The presence of steps on the bottom of the planing hull leads to the formation of air cavities in the bottom and significantly reduces the frictional resistance. Several experimental, analytical, and numerical research have been performed on transverse steps. Makasyeyev (2009) proposed a mathematical method

✉ Parviz Ghadimi
pghadimi@aut.ac.ir

1   Department of Maritime Engineering, Amirkabir University of Technology, Hafez Ave, No 424, P.O. Box 15875-4413, Tehran, Iran

to predict the air cavity formed behind the step, based on the dimensionless numbers of Froude and Cavitation and other effective features. Matveev (2012) used a sink and source method to simulate a two-dimensional planing hull. He stated that the most important factors influencing the shape of the cavity are the number, height, and position of the steps. Brizzolara and Federici (2010) have also examined the effect of the presence of air cavities in hydrodynamic behavior of stepped planing hulls by comparing stepped and non-stepped models. In 2009, Savitsky (2010) conducted some extensive experiments on several types of single-step mono-hulls to provide empirical formulas for prediction of wake profiles in different deadrise angles. The results of this research are semi-empirical formulas based on the results of conducted tests. These relations facilitate the design conditions of stepped hulls. They can be used for specific ranges of parameters such as trim angle, velocity coefficient, and load factor of these type of vessels.

Numerical simulation is a conventional method of predicting the hydrodynamic behavior of a vessel. In this method, by eliminating human errors and the cost of testing, or the complex process of solving equations in the mathematical methods, an accurate solution is obtained in a shorter time and at a lower cost. Also, many hydrodynamic details that cannot be obtained using experiments or mathematical methods can be easily presented using numerical simulation. Therefore, many researchers have used a variety of numerical methods to study the hydrodynamics of planing hulls (Shademani and Ghadimi 2017a, b, c, d; Sajedi et al. 2019; Doustdar and Kazemi 2019; Lotfi et al. 2015). In 2012, Garland and Maki (Garland and Maki 2012) conducted a study on two-dimensional stepped planing hulls that examined the optimal height of step for maximum possible lift. Numerical studies on the hydrodynamics of single-step planing hulls were also followed by some other researchers (Brizzolara and Federici 2013; Fu et al. 2014). Hay et al. (2006) conducted a study in which they simulated a two-phase flow around moving objects using dynamic mesh method. This numerical method was used to calculate the unstable flow around a prismatic body that collided with the water surface, symmetrically, and asymmetrically. The very high validity of the results determined the applicability of the mentioned method for accurate free surface modeling. Ghadimi et al. (2014) presented a parametric study by providing a computer program. They examined the position and three-dimensional profile of the spray. Taunton et al. (2010) studied a new series of hard chine planing hulls in an experimental study in calm water and the presence of waves. In these experiments, three models of a same vessel were studied in stepless, single-step, and double-step modes. Vitiello et al. (2012), Lee et al. (2014), and Svahn (2009) are researchers who have worked experimentally and numerically on one and double-step vessels. Cucinotta et al. (2017) investigated the effect of

bubble injection on hydrodynamic performance and drag of single-step high-speed mono-hulls. De Marco et al. (2017) examined the flow pattern around the vessel and examined the effect of step on hydrodynamic behavior of a vessel. On the other hand, some research has been done on the stability of stepped planing hulls. If the left and right sides of the step are not ventilated in the same way, a yaw motion could be applied to the vessel by the fluid, which can eliminate the stability (Timmins 2014; Ghadimi and Panahi 2018, 2019). Another valuable study that has been done on stepped planing hulls is the study of the effect of loading and deadrise angle on the vessel. The performance of a stepped planing hull could reduce by an incorrect selection of the center of gravity and weight distribution (Kazemi and Salari 2017; Konstantin et al. 2015). Afriantoni et al. (2020) studied the stability of high-speed craft with hull angle variations.

According to the presented literature review, providing step(s) in a planing hull usually reduces resistance. However, no comprehensive study has been performed on the effect of different shapes of steps on stepped planing hulls. So far, the effect of the angle of the various steps on the performance of the planing hull has not been studied and compared. Therefore, in the current paper, four planing models with different forms of step are investigated experimentally and numerically. The numerical simulation is conducted in two degrees of freedom, namely the motions of heave and pitch using Star CCM + software. Among these four models, the first model is a non-step model, and the other three models are equipped with transverse step, pointed aft step, and re-entrant Vee step, respectively. The aim of this study is to investigate the effect of step shape and angle on mono-hull planing-hull performance. This paper compares hydrodynamic parameters such as drag, trim, and rise-up. In numerical simulation, the pressure contours, wave pattern, and wake of different models are compared with each other.

2 Problem Definition

Three types of step forms are used in high-speed vessels. The first type of step is flat and is known as the transverse step. The second and third forms of the steps are angled, which are called pointed aft and re-entrant Vee step. Figure 1 shows these three forms of steps, along with a view of the bottom of the non-step model.

Until recently, the stepped vessels used mostly flat steps. However, nowadays, the use of angled steps is more common. The primary reason for this increase is proper ventilation of these types of steps while the vessel is moving. In this paper, the performances of these three types of steps are compared.

Fig. 1 Model A: non-step—
model B: transverse step—
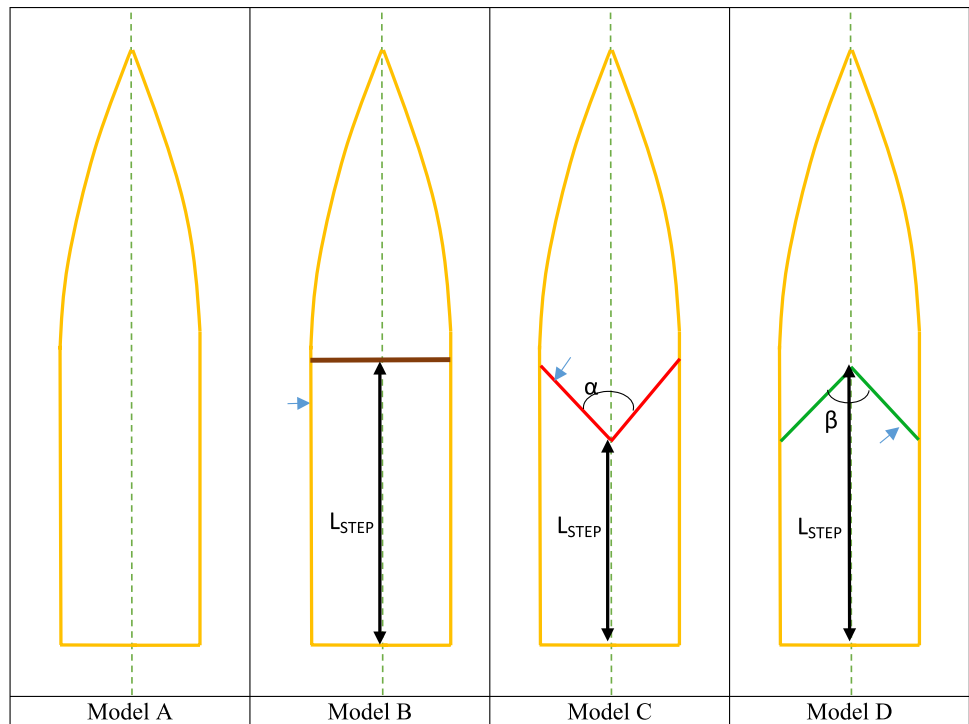model C: pointed aft step—
model D: re-entrant Vee step

Table 1 Principal characteristic of the investigated models

Model	L_{STEP}	α or β	Dead deg
Model A	No step	No deg	24
Model B	720	180	24
Model C	680	154	24
Model D	720	154	24

3 Introducing Test Models

In the present paper, four planing hull models are studied, experimentally. All models are similar and differ only in the shape of steps. These models are made based on a hard-chine planing-hull prototype and are shown in Fig. 1. The length, width, and weight of these models are 2640 mm, 551 mm, and 86 kg, respectively. The distance from the center of gravity of the models to their aft is

791 mm. The weight factor (CD) is equal to 0.5. Table 1 shows the full specifications of these models.

Figure 2 shows a body plan view of model A. The models are based on a Cougar vessel prototype and are modeled on a 1: 5 scale. The deadrise angle of these models in the aft is 24°. The height of the steps of these models is 25 mm, which is about 4% of their width. This percentage is in the range of height-to-width ratio of the investigated models in some experimental and numerical research done in different papers. Table 2 provides a comparison between this ratio in some well-known studies.

3.1 Description of Experiments

The experiments are conducted in the towing tank of the National Persian Gulf Marine Laboratory. The main specifications of this laboratory are given in Table 3. All tests are performed according to ITTC recommendations. All experiments conducted performed in calm water with a
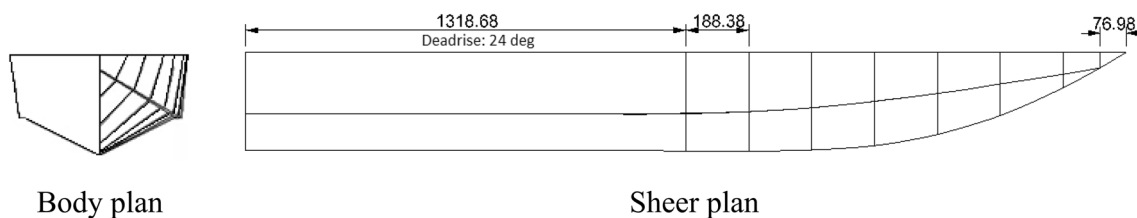

Body plan   Sheer plan

Fig. 2 Body lines of model A

Table 2 Height-to-width ratio of step in some well-known experimental studies

The percentage of height step to Beam	Work
2, 4, 6,8	Garland and Maki
4	Taunton
5.8, 10, 14.4	Radestrom

Table 3 Dimensions and features of towing tank

Variable	Value
Length (m)	392
Water depth (m)	4
Width (m)	6
Maximum capacity of the force gauge (N)	600
Maximum measurement ranges of the potentiometer (°)	± 30

The uncertainty condition for resistance and trim is calculated according to Eqs. 2 and 3.

$$U_{CT}{}^2 = \left(U_{\boldsymbol{B}\,CT}^{\,Tw}\right)^2 + \left(K.U_{P_{CT}}\right)^2 \tag{2}$$

$$\left(U_\tau\right)^2 = \left(B_\tau\right)^2 + \left(P_\tau\right)^2 \tag{3}$$

Equations 2 and 3 represent uncertainties of total drag and total trim, respectively. These two quantities are calculated based on the total drag coefficient and trim of the models, respectively. The results of calculations performed for model A (without step) are given in Table 5.

3.2 Experimental test results

Table 6 shows the measured trim and drag from the experiments of models A, B, C, and D in the towing tank. Figure 4 shows images taken by a video camera connected to
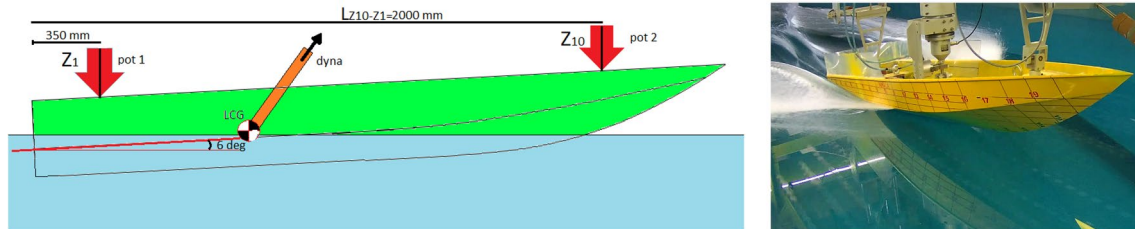
Fig. 3 Location of sensors on the models

temperature of 293 K, a density of 1002 kg/m³, and a viscosity of 1.9E−6 m²/s. The maximum speed of the carriage is 19 m/s, and it has two different speed modes. Low-speed mode covers speeds from 0 to 5 m/s, and the high-speed mode ranges from 5 to 19 m/s. Three sensors are installed on the models to determine the resistance, trim, and rise-up.

Figure 3 shows a view of the installation of the sensors on the model. The models are attached to the carriage and towed at the intersection of the shaft direction with the center of gravity. The angle of the shaft direction with the horizon is 6°, and the distance of the center of gravity from the aft of the model is 791 mm. Figure 3 shows two potentiometers and one dynamometer.

Potentiometers 1 and 2 measure the value of rise-up in two different positions, and the value of the center of gravity is calculated using simple mathematical calculations as in

$$\tau = \tan^{-1}\left(\frac{Z_{10} - Z_1}{L_{10-1}}\right) \tag{1}$$

Table 4 also shows the error associated with the sensors and laboratory meters.

Table 4 Error values in laboratory sensors

Parameter	Error
Resistance dynamometer	0.02 FS %
Construction of model	1 mm
thermometer	0.1 °C
Measurement of sinkage and rise-up	1 mm

Table 5 The uncertainty for model A

V m/s	Drag %	Trim %
1	1.2367	1.771
2	0.3098	.998
3	0.3908	0.345
4	0.3496	0.566
5	0.4372	0.437
6	0.3895	0.241
7	0.2041	0.227

the carriage.

Table 6 Measured parameters for models A, B, C, and D

U m/s	Fr	Model A			Model B		Model C		Model D	
		Z_{CG} (mm)	τ (°)	R_T (KgF)	τ (°)	R_T (KgF)	τ (°)	R_T (KgF)	τ (°)	R_T (KgF)
1	0.21	− 1.78	2.47	0.8	3	1.3	3	1.2	3	1.3
2	0.43	− 8.67	3.73	5.4	4.2	6.2	4.1	6	4.2	6.2
3	0.64	4.03	6.17	11.55	6.4	12.3	6.3	12.46	6.2	13.12
4	0.85	26.71	6.77	13.05	6.6	13.4	6.4	13.29	6.5	14.42
5	1.07	52.61	7.39	13.94	6.2	13.8	6.3	13.6	6.2	14.53
6	1.28	70.26	6.63	13.65	5	13.36	5.1	13.1	5	13.51
7	1.49	81.54	5.81	13.8	4.5	13.54	4.3	13.2	4.2	13.7
8	1.71	PORP	PORP	PORP	4	14.38	3.8	13.75	3.8	14.5
9	1.92	PORP	PORP	PORP	3.2	15.39	3.5	14.66	3.3	15.7

Fig. 4 Dry surface area below the stepped models at the speed of 9 m/s, **a** model B, **b** model C, **c** model D

a   b   C
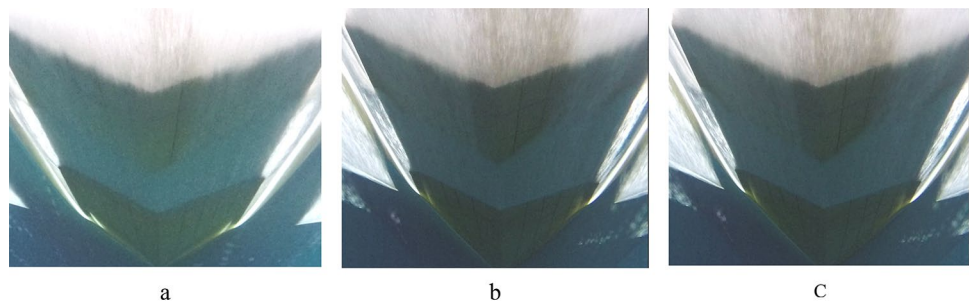
The results of test model A show that at speeds above 8 m/s, the porpoising phenomenon occurs. However, the results of other test models show that they are stable with the help of steps. The reason for this stability is the proper pressure distribution at the bottom of the stepped models. Model C has the lowest resistance and the highest dry surface area due to proper ventilation. On the other hand, model D has the highest resistance among the tested models due to lack of proper ventilation. Of course, all stepped models are stable and porpoising is avoided at any speed. Figure 4 shows a view of models B, C, and D.

Subsequently, numerical simulations are performed in Star CCM + software. With the help of experimental data, the numerical results are validated and finally the pointed aft and re-entrant steps are modeled with different angles to extract the optimal angle.

4 Numerical Simulation

4.1 Governing Equations of Turbulent Flow

First, equations are written for instantaneous quantities, that is, time-averaged quantities along with oscillating quantities. Then, each side of the equation is averaged over time. It should be noted that if there is an equation for instantaneous quantities, this equation will also be established for its time average (for a specific range of time). Finally, equations can

be simplified to the point where time-averaged quantities appear. As a result, the following statement is obtained for compressible flow:

$$\frac{\partial}{\partial x_i}\left(\overline{\rho u_i}\right) + \frac{\partial}{\partial x_i}(\overline{p'u'_i}) = 0 \tag{4}$$

Since $\rho' = 0$, the above equation for the incompressible flow is as follows:

$$\frac{\partial \overline{u_i}}{\partial x_i} = 0 \tag{5}$$

$$\rho\left[\frac{\partial \overline{u_i}}{\partial t} + \overline{u_j}\frac{\partial \overline{u_i}}{\partial x_j}\right] = \overline{B_l} - \frac{\partial \overline{p}}{\partial x_i} + \frac{\partial}{\partial x_j}\left[\mu\frac{\partial \overline{u_i}}{\partial t} - \rho\overline{u'_i u'_j}\right] \tag{6}$$

The only difference between the above momentum equation and the momentum equation with instantaneous quantities is the addition of the last term, $\rho\overline{u'_i u'_j}$, on the right side of the equation. This term is called turbulent tension or Reynolds tension. The only difference between laminar flow and turbulent flow equations is the presence of this term. In general, this term is not a physical tension, but an effect of inertia (momentum) exchange. It should be noted that this term has been moved to the right from the left side of the momentum equation, where there are inertial expressions.

On the other hand, Reynolds stress tensor, $(\overline{u'_i u'_j})$, is based on Boussinesq's hypothesis:

$$\overline{u'_i u'_j} = v_t \left(\frac{\partial U_i}{\partial x_j} + \frac{\partial U_j}{\partial x_i} \right) + \frac{2}{3} \delta_{ij} k \tag{7}$$

In the above relation, v_t represents the vortex viscosity used in the standard $k - \epsilon$ turbulence model. This parameter is obtained using the relation $v_t = C_\mu \frac{k^2}{\epsilon}$, where C_μ is an empirical constant and is assumed 0.99. The parameters of k and ϵ also represent the kinematic energy of the turbulence and the scattering rate of k, respectively. These two parameters are obtained using the standard $k - \epsilon$ turbulence model. Standard $k - \epsilon$ is a two-equation model that uses the following transfer equations to express the turbulent properties of the flow.

$$\frac{\partial k}{\partial t} + \frac{\partial}{\partial x_i}\left(k\overline{U_i} \right) = \frac{\partial}{\partial x_i}\left[\left(v + \frac{v_t}{\sigma_k} \right) \frac{\partial k}{\partial x_i} \right] + P_k - \epsilon \tag{8}$$

$$\frac{\partial \epsilon}{\partial t} + \frac{\partial}{\partial x_i}\left(\epsilon\overline{U_i} \right) = \frac{\partial}{\partial x_i}\left[\left(v + \frac{v_t}{\sigma_\epsilon} \right) \frac{\partial \epsilon}{\partial x_j} \right] + \frac{\epsilon}{k}\left(C_{\epsilon 1}P_k - C_{\epsilon 2}\epsilon \right) \tag{9}$$

These two equations consist of four adjustable constants of $C_{\epsilon 1} = 0.44$, $C_{\epsilon 2} = 1.92$ and turbulent Prandtl numbers of k and ϵ, that is $\sigma_k = 1$ and $\sigma_\epsilon = 1.3$.

4.2 Volume of Fluid (VOF) Model

Volume of Fluid model is used to simulate free surface. This model uses a concept called equivalent fluid. Here, it is assumed that the (two) phases of the fluid share the same velocity and pressure. This ultimately allows them to be solved as a single-phase flow with the same set of governing equations of momentum and mass described in the previous section. Volumetric fraction, α_i, of phase i describes which cell surface is filled with the corresponding fluid (Afriantoni et al. 2020).

$$\alpha_i = \frac{V_i}{V} \tag{10}$$

The fluid volume method is appropriate when the provided grid is dense enough to resolve the connection between the two non-mixed fluids, and this model is a simple multiphase model. As observed in Fig. 5, where the volume fraction value is 0.5, the free surface is defined as a boundary. It should be noted that this location is not at the center of the control volume, but the geometric values (Mancini 2015).

An additional equation called volume fraction convention equation is added to the mass and momentum equations to simulate the dynamics of the waves. Assuming that the flow is incompressible, this equation is defined as follows (Mancini 2015):
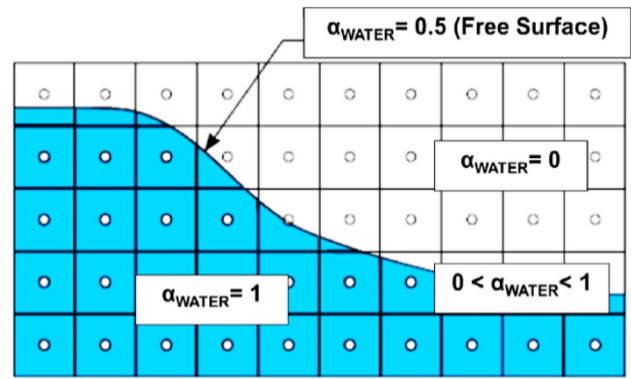

Fig. 5 The basis of the fluid volume fraction method (CD-Adapco 2017)

$$\frac{\partial}{\partial t}\int_V \alpha_i \mathrm{d}V + \int_V \alpha_i (V - V_b)n\mathrm{d}S = 0 \tag{11}$$

The physical properties of the equivalent fluid inside a control volume are calculated as functions of the physical properties (density and viscosity) of the phases and their volumetric fractions (Mancini 2015).

$$\begin{cases} \rho = \sum_i \rho_i \alpha_i \\ \mu = \sum_i \mu_i \alpha_i \\ 1 = \sum_i \alpha_i \end{cases} \tag{12}$$

4.3 Methods in CFD Simulation

To achieve high accuracy in software simulations, it is necessary to perform precise geometry modeling, to properly select the computational domain, meshing, determination of boundary and initial conditions, selection of appropriate solver and time step. In the present paper, the simulation is based on the parameters presented in Table 7.

To properly estimate all the unknown hydrodynamic parameters at each time step, the RANS equations are solved in implicit unsteady and iterative manner. The coupled pressure–velocity and the whole solution process are based on the SIMPLE method. The selected turbulence model is $k - \epsilon$. The simulation is done in two degrees of freedom, namely the heave and pitch motions. These degrees of freedom are simulated using the dynamic fluid-body interaction (DFBI) model of the software. The RANS solver computes the forces and moments exerted on the models. This model also solves the motion equations and computes the displacements, velocities, and linear as well as angular accelerations relative to the coordinate system connected to the vessel. On the other hand, due to the transitional and rotational motions of the models, a moving domain, connected to the

Table 7 Specifications of CFD simulation

| Parameter	Value
Solver	Implicit, unsteady
Free surfaces modeling	Volume of fluid (VOF) method via high resolution interface capturing (HRIC)
Pressure–velocity coupling	Semi-implicit method for pressure linked equation (SIMPLE)
Convection term	Second-order SIMPLE
Diffusion term	Central difference scheme
Time discretization	Second order fully implicit approach
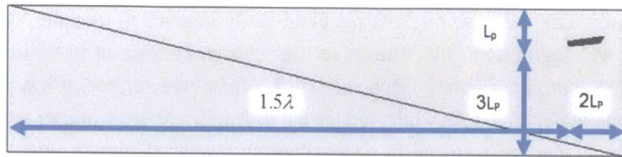
Fig. 6 Selection pattern of computational domain (Failed 2014)

model inside a stationary domain, is required. The mesh changing in the overset dynamic mesh method is more suitable for monitoring the severe heave and pitch motions than the morphing method. The two-phase flow, which includes water and air, is solved using the VOF model and is based on tracking the free surface boundary.

Studies show that the size of computational domain and the distance of the model from its boundaries greatly affect the accuracy of the results. In fact, the domain boundaries should be far enough away from the model so that the effects of the model geometry on the flow do not affect the domain boundaries. According to ITTC recommendation of 2011 (ITTC 2008a), the distance from the back boundary to the hull should be between 3 and 5 times the length of the model, and the distance between the upstream, top, bottom and sides to the hull should be between one and two times the length of the model. Also, to increase the accuracy of results and Kelvin wave pattern around the

model, a control volume in the shape of a cone with an angle of 19.28° has been created. The center of this control volume is the free surface, and smaller cells are used in this region. Figure 6 shows one of the options proposed by Sheingart (2014) to create a computational domain. In this figure, L_P is the length of the vessel, and λ is calculated using Eq. (13). The U parameter also indicates the horizontal component of the flow velocity.

$$\lambda \approx 2\pi \frac{U^2}{g} \tag{13}$$

The general computational domain, as shown in Fig. 6, is a rectangular cube whose length depends on the model velocity. Based on Eq. 17, with increasing speed, the domain length must also increase. Therefore, in the present paper, all simulations are performed in a computational domain with dimensions proportional to the highest speed examined. Figure 7 shows a view of this computational domain. The length overall (LOA) of the model is assumed to be 2.64 m. The next important step in simulation process is to apply the boundary conditions of the problem. In the simulation process, due to the high computational cost, half of the model is modeled, and the symmetry condition is applied. As observed in Fig. 7, the upstream and downstream boundaries are velocity inlet and pressure outlet, respectively. The model is considered a no-slip wall, and

Fig. 7 Computational domain
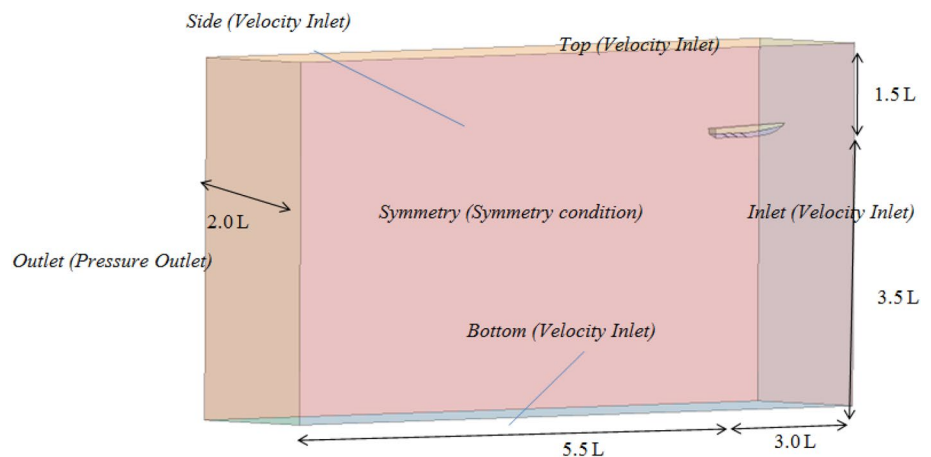
the conditions of the upper and bottom sides are velocity inlet.

The discretization of the computational domain is performed using a structured mesh with quadrilateral (hexagonal) cells. This type of mesh is the most suitable and high-quality option to model complex two-phase problems and is used for external flows. The process of selecting the size of the mesh is done in relation to a base value, and then, the required corrections are made around the model, step, moving domain, and free surface. The top, front, and side views of the mesh, as well as the boundary layer around the stepped model, are shown in Fig. 8.

An important criterion that should be considered in the production of the grid within the boundary layer is y^+, which refers to the dimensionless distance of the first node of the mesh from the surface. Using the standard turbulence model of $k - \epsilon$, which consists of two equations, a series of additional wall functions are required to obtain the relations of the variables between the wall and the totally turbulent region. The velocity in this region changes logarithmically relative to y^+ (Eq. 14). Under the Stanford Convention, the von Karman constant is defined as $K = 0.41$ and $B = 5$ (ITTC 2008a).

$$U^+ = \frac{1}{\kappa}\ln(y^+) + B \tag{14}$$

U^+ is the dimensionless velocity of flow and a function of the frictional velocity, u_t. Another point to note is the choice of time step (Δt) according to Eq. 19, which is expressed as a function of length (l) and velocity (V) based on the ITTC recommendation of 2008 (ITTC 2011). Here, this length is assumed to be equal to the wetted length of the keel (L_k) of the model.

$$\Delta t = 0.01 \sim 0.005 \frac{l}{V} \tag{15}$$

It should also be noted that the Courant number (CFL) remains below 1 as a function of the time step, speed, and minimum element length in the direction of fluid flow. Equation 16 defines the Courant number.

$$C = \frac{V_i \cdot \Delta t}{\Delta x_i} \leq C_{\max} \tag{16}$$

Δx is the distance of the first cell, the smallest cell, from the body surface. Of course, the Courant number changes as the Froud number changes.

4.4 Validation

Validation of drag, trim, and rise-up calculations of model B for three different types of structured trimmer hexahedral dynamic mesh is performed at a Froude number of 1.97 (speed of 9 m/s). Table 8 shows the calculated resistance of model B for different mesh at 9 m/s speed. It is observed that by increasing the number of cells to more than 1.7×10^6, there are no significant changes in the resistance force, and therefore, this number of cells is suitable for this simulation.

Table 8 Accuracy of the computed resistance using different numbers of cells

Grid accumulation	Num. mesh $\times 10^6$	Numerical dreg
Coarse	15	16.8
Medium	17	14.5
Fine	29	14.9
Difference percentage	Coarse to medium	13%
	Medium to fine	2%

Fig. 8 The top, front, and side views of the mesh and the boundary layer around the stepped model
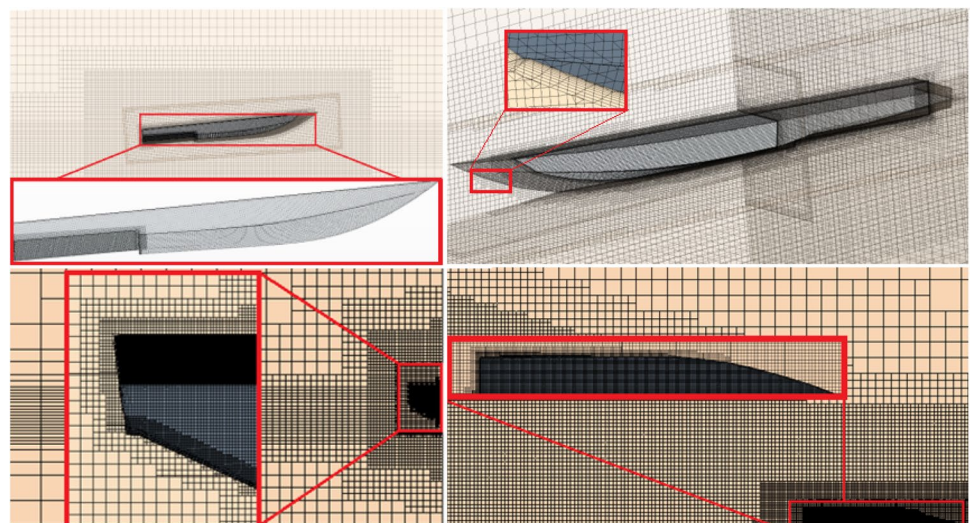
Uncertainty of numerical simulation at this speed can be determined based on the method provided by Wilson et al. (2001). Recommendation of ITTC in 2008 (2008b) explains that the U_{SN} numerical simulation uncertainty consists of three different uncertainties: repetition, U_I, grid, U_G, and time stack, U_{TS}. Equation 17 calculates the overall uncertainty of the simulation:

$$U_{SN}^2 = U_I^2 + U_G^2 + U_{TS}^2 \tag{17}$$

According to Wilson et al. (2001), the most critical source of numerical simulation uncertainty is grid uncertainty. Therefore, as presented in Table 8, the grid convergence Index (GCI) of three different grids has been calculated using the reliability factor of 1.25 proposed by Roache (2002). Studies show that the convergence coefficient, $R_K = \varepsilon_{21_K}/\varepsilon_{32_K}$, is in the range of $0 < R_K < 1$, so it satisfies the monotonic convergence. In this method, the average value of apparent order is calculated using Eq. 22.

$$P_{avg} = \frac{1}{\ln(r_{21})}\left|\ln\left|\varepsilon_{32}/\varepsilon_{21}\right| + q(P_{avg})\right| \tag{18}$$

where

$$q(P_{avg}) = \ln\left(\frac{r_{21}^{P_{avg}} - s}{r_{32}^{P_{avg}} - s}\right) \tag{19}$$

In the present study, mesh correction factors are $r_{21} = \sqrt{2}$ and $r_{32} = \sqrt{2}$. Besides, for the calculated parameters such as trim, drag, and rise-up, which are denoted by φ, there are two relations of $\varepsilon_{21} = \varphi_2 - \varphi$ and $\varepsilon_{32} = \varphi_3 - \varphi_2$, which are given in Eq. 18. Subsequently, four parameters of extrapolated value, defined approximated relative error, extrapolated relative error, and fine-grid convergence index, are defined in Eqs. 20–23, respectively. These parameters are all used in the calculation of the ultimate value of GCI. Defined parameters are obtained for intended hydrodynamics resistance in Table 9.

$$\varphi_{ext}^{32} = \left(r_{32}^{P_{avg}}\varphi_2 - \varphi_3\right)/\left(r_{32}^{P_{avg}} - 1\right) \tag{20}$$

$$e_a^{32} = \left|\frac{\varphi_2 - \varphi_3}{\varphi_2}\right| \tag{21}$$

$$e_{ext}^{32} = \left|\frac{\varphi_{ext}^{23} - \varphi_2}{\varphi_{ext}^{23}}\right| \tag{22}$$

$$GCI_{fine}^{32} = \frac{1.25 e_a^{32}}{r_{32}^{P_{avg}} - 1} \tag{23}$$

Table 9 CGI method for hydrodynamics resistance

Parameter	Hydrodynamics resistance (N)
φ_1	164
φ_2	142
φ_3	146
P_{avg}	5.6
φ_{ext}^{32}	201.96
e_a^{32}	0.314%
e_{ext}^{32}	0.081%
GCI_{fine}^{32}	6.854%

Table 10 compares the results of the simulation of stepped models at two speeds of 8 and 9 m/s with the corresponding experimental measurements.

Figure 9 displays the y^+ value at the bottom of the models. These values are for models B and C at speeds of 8, 9 and 10 m/s. As evident in Fig. 9, these values of y^+ are all less than 100, which is acceptable according to the selected turbulence model.

4.5 Simulation and Numerical Results

4.5.1 Trim, Rise-Up, and Drag

In addition to the steps used in the experimental study, other types of steps have been modeled to examine the effect of step shape on the performance of models. Table 11 shows the main specifications of all types of steps studied in the present paper. The three steps, which were first tested, are given the same name in this table and are marked in dark color. Figure 10 is presented to provide a proper understanding of the values given in Table 11.

Simulations are conducted at three speeds of 8, 9, and 10 m/s. The results of rise-up, trim and drag are given separately in Tables 12, 13, 15 and 16. In three angles of 156°, 134° and 114°, the performance of stepped vessels has been investigated.

Among the three models of B0, B, and B1, the drag of model B is the lowest. This is because the trim and rise-up of this model are more than those of other models. Model B, on the other hand, has the highest drag and the lowest rise-up. Figure 11 shows the trim, drag, and rise-up at three speeds for the three models equipped with a transverse step.

In general, by decreasing the angle in three positions of B0, B, and B1, the drag is reduced. As the angle decreases, the trim and rise-up also decrease. The model equipped with a pointed aft step has less drag than the model equipped with a transverse step. One of the reasons for this reduction is the proper ventilation of the pointed aft step. All models equipped with pointed aft steps with different angles, at three

Table 10 Comparison of experimental and numerical results at the speeds of 8 and 9 m/s

Model	Velocity	Total drag			Trim		
		Exp	Num	Error %	Exp	Num	Error %
B	8	14.38	14.56	1	4	4.3	7
B	9	15.39	14.48	5	3.2	3.6	12
C	8	13.75	13.67	0.5	3.8	4.1	7
C	9	14.66	14.38	1	3.5	3.7	5
D	9	15.7	14.61	6	3.3	3.7	12
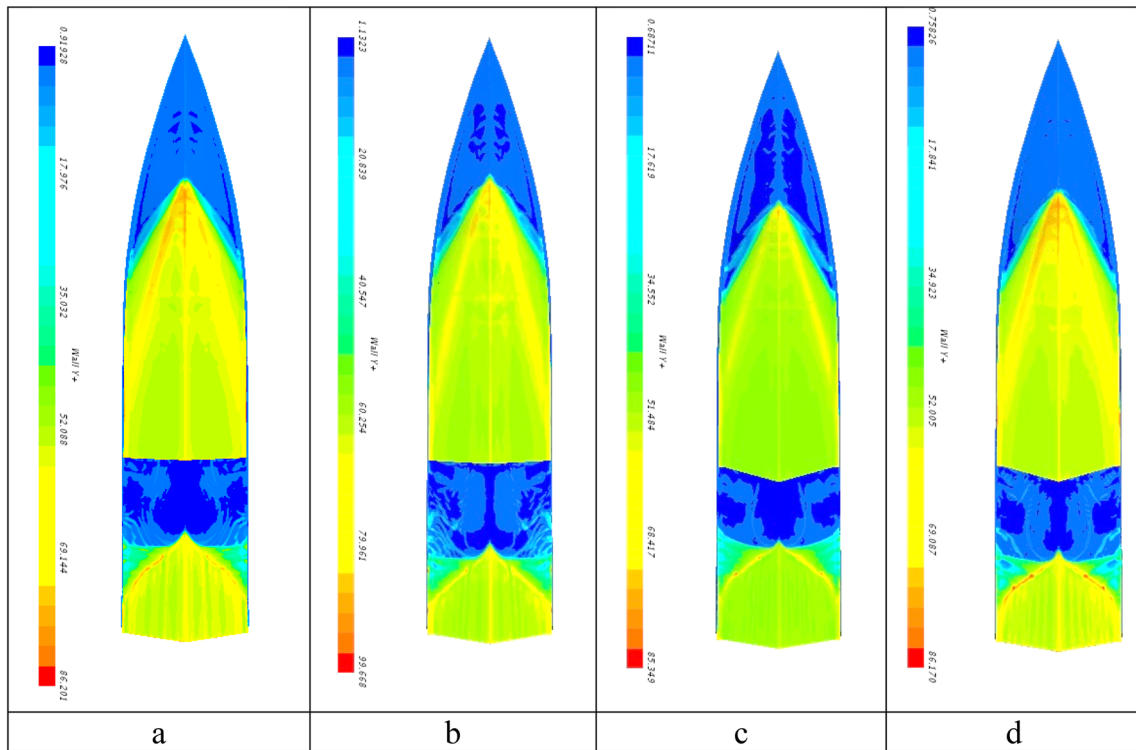
Fig. 9 The value of y^+ for model B at the speeds of **a** 9 m/s, and **b** 10 m/s, and for model C at the speeds of **c** 9 m/s, and **d** 10 m/s

Table 11 Numerical models

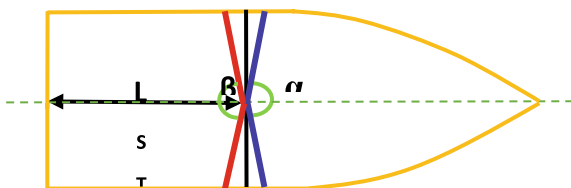| Step from transon (mm)	Transverse Step	α Step pointed Aft			β Re-entrant Vee	
670	B 0	156	134	114	156	134
720	B	156	134	114	156	134
770	B 1	156	134	114	156	134

Fig. 10 Identifying the parameters used in Table 11

speeds of 8, 9, and 10 m/s, exhibit less drag than the models equipped with transverse steps. Tables 14 and 15 show the numerical results of the resistance, trim, and rise-up of the models equipped with pointed aft steps at speeds of 9 and 10 m/s.

As observed in Tables 13, 14, and 15, drag decreases as the trim angle and rise-up decrease.

Figures 12, 13, and 14 show the effect of step length on drag, trim, and rise-up. If the step is as much as 27% of

Table 12 Computed resistance, trim, and rise-up of the models equipped with a transverse step

Step type	The distance of the steps from the transom	L_{STEP}/ LOA (%)	8 m/s			9 m/s			10 m/s		
			R	τ	Rise. UP	R	τ	Rise. UP	R	τ	Rise. UP
B 0	670	25	13.87	4.3	82	14.04	3.78	86	14.85	3.55	93
B	720	27	13.87	4.09	79	14.49	3.62	84.9	15	3.19	88
B 1	770	29	14.28	4.1	79	14.36	3.5	84	15.3	3	85

Table 13 Computed resistance, trim, and rise-up of the models equipped with a pointed aft step at a speed of 8 m/s

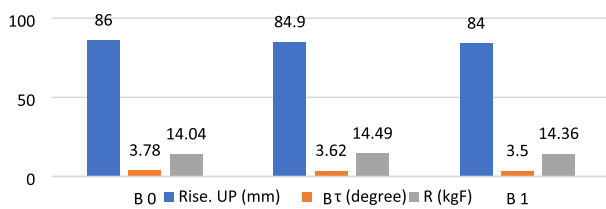| Step type	Drag at 8 m/s			Trim at 8 m/s			Rise-up at 8 m/s		
	156	134	114	156	134	114	156	134	114
B 0	13.67	13.67	13.67	4.16	4.13	4.1	80	79.7	79
B	13.81	13.69	13.61	4.08	4.08	4.05	79	79	78
B 1	13.9	13.77	13.65	4.03	4.01	4	78	78	76

Fig. 11 Comparison of drag, trim, and rise-up of models equipped with a transverse step at 9 m/s speed

of the location of this type of step on the performance of the model can be predicted. The three positions on which the pointed aft steps are mounted, B0, B, and B1 are 25, 27, and 29% of the model's length to the aft of the models, respectively. Also, the pointed aft step in each of the positions of B0, B, and B1 is studied at three angles of 156, 134, and 114, respectively.

The diagrams in Figs. 12, 13 and 14 show that a location must be specified according to the specific gravity center to select the appropriate step. This optimal location

Table 14 Computed resistance of resistance, trim and rise-up of the models equipped with pointed aft step at a speed of 9 m/s

Step type	Drag at 9 m/s			Trim at 9 m/s			Rise-up at 9 m/s		
	156	134	114	156	134	114	156	134	114
B 0	14.38	14.32	14.06	3.7	3.69	3.64	86	85.8	85
B	14.18	13.97	13.87	3.64	3.65	3.53	85.1	85.1	83.5
B 1	14.28	14.28	14.18	3.47	3.44	3.44	83	82.1	81.9

Table 15 Computed resistance of resistance, trim and rise-up of the models equipped with pointed aft at a speed of 10 m/s

Step type	Drag at 10 m/s			Trim at 10 m/s			Rise-up at 10 m/s		
	156	134	114	156	134	114	156	134	114
B 0	14.83	14.77	14.69	3.28	3.27	3.23	89	88	88
B	14.79	14.69	14.59	3.2	3.23	3.15	88	88	87
B 1	14.97	14.7	14.65	3.14	3.13	3	87.4	86	85

the vessel length away from the aft of the vessel, the best performance is achieved. In model B, which has the lowest drag, step is at such a distance from the aft of the model. The lowest and highest values of trim and rise-up are also provided in B1 and B0 models, respectively.

The performance of models equipped with pointed aft steps is shown in two ways in Figs. 12, 13, 14 and 15. Figures 12, 13 and 14 show the trim, drag, and rise-up values of these models. By comparing these diagrams, the effect

will definitely provide the best ventilation for the steps. Of course, this optimal location may not be the same as the optimal transverse step location. In general, the efficiency of angled steps is higher than the transverse steps. Figure 15 shows the effect of the step angle on the performance of the vessel. Figure 15a–c represents the performance of models whose steps are in positions B0, B, and B1, respectively.
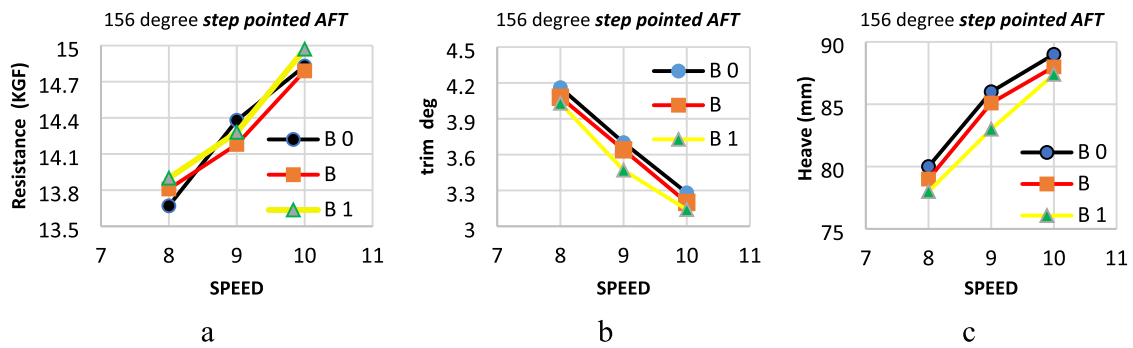
Fig. 12 Effect of the position of pointed aft step at an angle of 156° on **a** drag, **b** trim, and **c** rise-up of the models
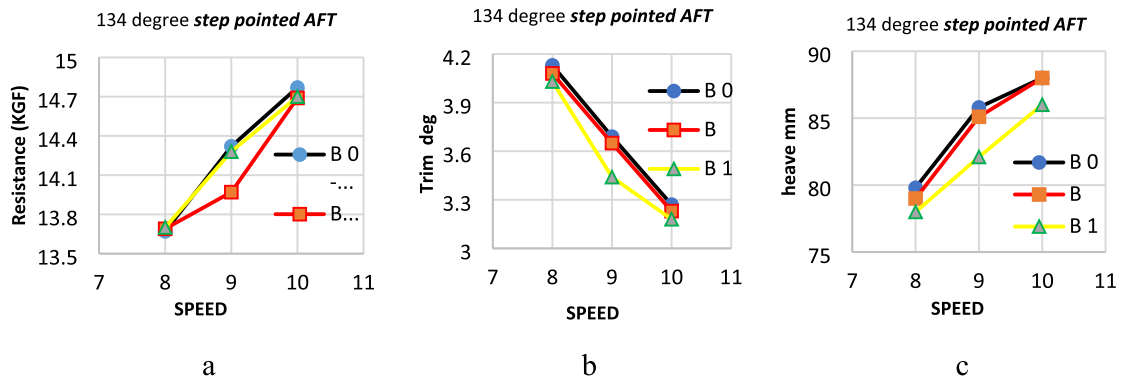

Fig. 13 Effect of the position of pointed aft step at an angle of 134° on **a** drag **b** trim **c** rise-up
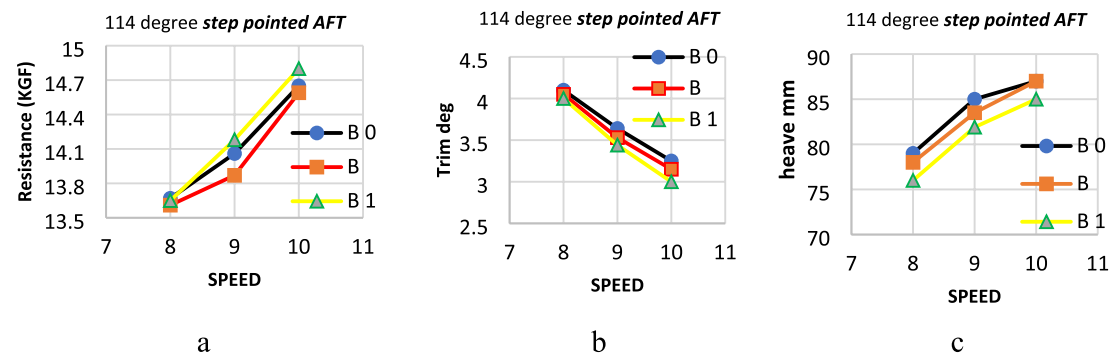

Fig. 14 Effect of the position of pointed aft step at an angle of 114° on **a** drag **b** trim **c** rise-up

As shown in Fig. 15, as the angle decreases, the drag of all three models equipped with pointed aft steps decreases, too. By reducing the angle, better ventilation is achieved at the bottom of the model. In fact, the lower the angle, the better the ventilation at the bottom of the model.

Figure 15a shows the results for models equipped with pointed aft steps, whose steps are provided in 25% of the model's length to the aft of the models at angles of 156,

134, and 114. The lowest and highest drag correspond to 114° and 156°, respectively.

The results of the models equipped with re-entrant Vee steps are presented in Table 16. The study is conducted at two locations with an angle of 156° for three speeds of 8, 9, and 10 m/s. The performance of this type of step is investigated for three speeds of 8, 9, and 10 m/s by creating it at different locations with an angle of 156°. The values of
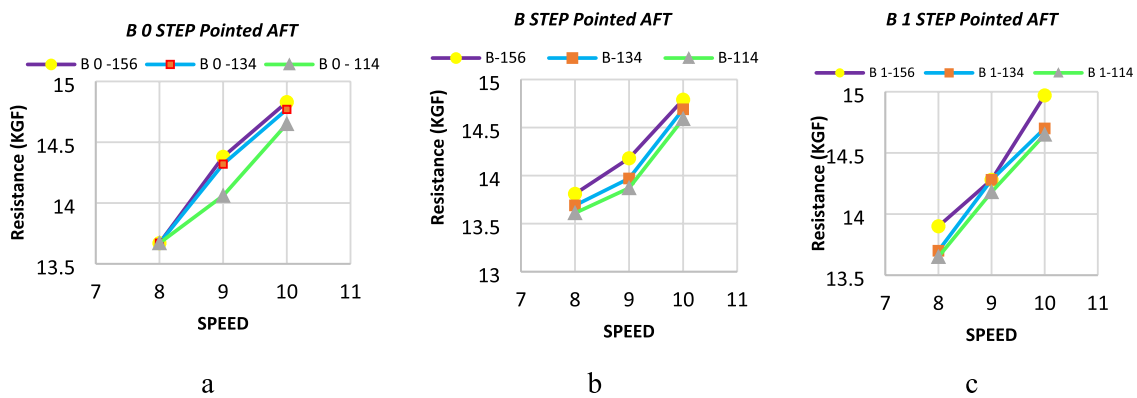
Fig. 15 Effect of angle on pointed aft steps in the positions of **a** B0, **b** B, and **c** B1

Table 16 Resistance, trim, and rise-up of models equipped with re-entrant Vee steps at a speed of 9 m/s and 10

Step type	9 m/s—156°			10 m/s—156°		
	R	τ	Rise. UP	R	τ	Rise. UP
B	14.61	3.71	86	15.2	3.27	89
B 1	14.59	3.6	84	15.12	3.2	88

trim, rise-up and drag of these models show that due to the inability of re-entrant Vee steps to provide proper ventilation, drag of the models equipped with these steps is higher than other stepped models studied in this article. The results of simulating these models are given in Table 16.

In general, it can be concluded that models equipped with pointed aft steps have a lower drag on the corresponding speeds than other stepped models. Meanwhile, the models equipped with transverse step and re-entrant Vee steps have less drag, respectively.

4.6 Pressure and Wetted Surface Area of the Bottom of Models

Figures 16 and 17 show the pressure contours and the wetted surface area of the bottom of the models, respectively. Figure 16 shows the pressure contour of models equipped with pointed aft step, for the placement of steps in three longitudinal locations of B0, B and B1 with an angle of 156° at speeds of 8 and 9 m/s. As the speed of the models increases, the momentum of water flow under the model, increases. As a result of this increase in speed and momentum, flow separation occurs. By increasing the flow separation, the stagnation line moves toward the aft of the model. As a result, the pressure moves backward, and the aft of the model pulls more out of the water, resulting in less trim angle. The lowest trim angle is related to the model equipped with pointed aft step in position B1.

The wetted surface area of the models equipped with pointed aft steps with three longitudinal locations of B0, B, and B1 has been shown in two speeds of 8 and 9 m/s in Fig. 17. As the speed of the model increases, the wetted surface area of its aft body decreases.

4.7 Wave Pattern and Positions of the Models

Wave pattern and rooster tail behind the models equipped with pointed aft step are illustrated in Fig. 18 at the speed of 9 m/s for positioning the steps at three different angles of 156, 134, and 114 and the best location, i.e., location B.

It is observed in Fig. 18 that, as the angle of the steps decreases, the rooster tail increases.

5 Conclusions

In this paper, four models of high-speed craft with different step shapes are studied experimentally and numerically. The effects of three types of steps, namely transverse step, pointed aft step, and re-entrant Vee step are examined. Hydrodynamic performance of these types of stepped models is compared with each other and with the non-step model. Numerical simulations are conducted in two degrees of freedom. Accordingly, the heave and pitch motions of these models are predicted by Star CCM + software. Comparison of the performance of these models are done through the computed drag, trim, and rise-up. Also, the pressure contours, wave pattern, and the wake formation behind the models are obtained using the numerical simulation. Based on the acquired results, one may conclude the followings:
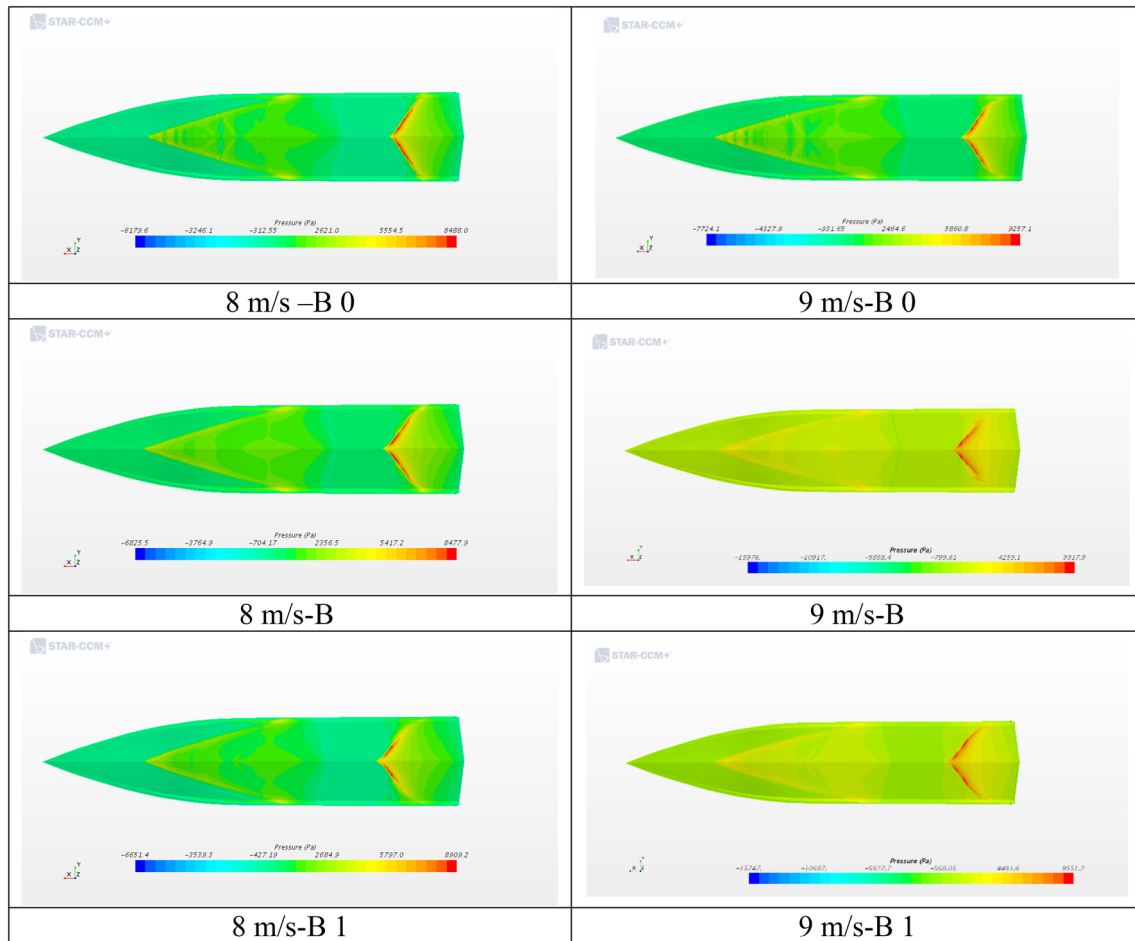
Fig. 16 Pressure contours on the bottom of the models equipped with pointed aft steps in three longitudinal positions of B0, B, and B1 and the angle of 156° in two speeds of 8, and 9 m/s

1- The non-step model is unstable longitudinally at the speed of 8 m/s and beyond, but all the stepped models are stable at all speeds.

2- The lowest resistance of the stepped models is obtained by using the pointed aft step. This reduction in drag is caused by two reasons: a decrease in wetted surface area and proper ventilation.

3- The highest drag is related to the non-step model and then to the model equipped with re-entrant vee step. The reason for this increase in drag is the lack of proper ventilation.

4- The effect of pointed aft step on the performance of the models is further studied numerically at three angles of 156°, 134°, and 114°. The results showed that at all speeds, the resistance decreases with decreasing angle.

5- Based on the obtained results from the experimental and numerical tests, the optimum case is the stepped hull equipped with the pointed aft step, which has the lowest step angle among all investigated models, i.e., 114°, and is located at 27% of the vessel length to the vessel aft.

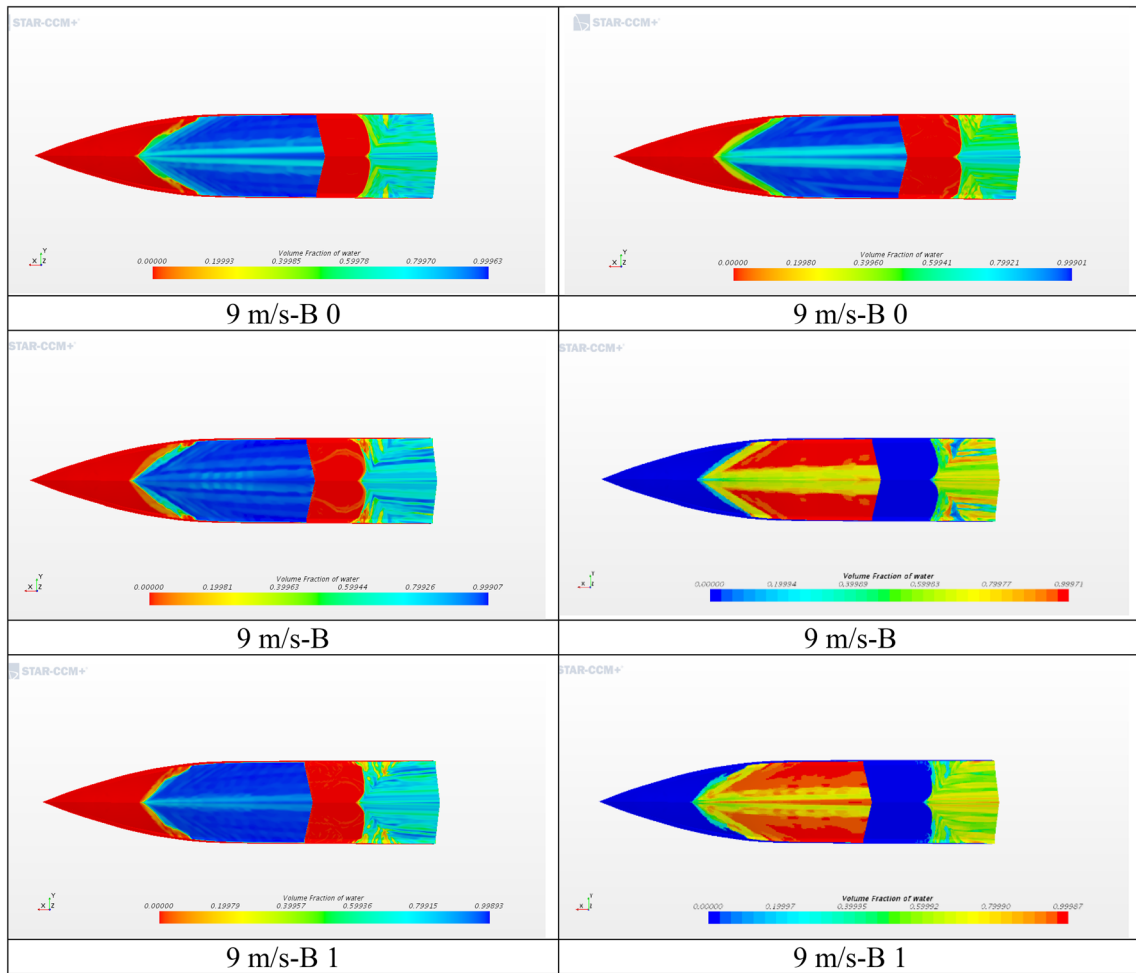6- By reducing the angle of the pointed aft step, the trim and rise-up are reduced.

Fig. 17 Volume fraction contour on the bottom of the models equipped with pointed aft steps for three longitudinal locations of B0, B, and B1, and at an angle of 156° at the speeds of 8 and 9 m/s
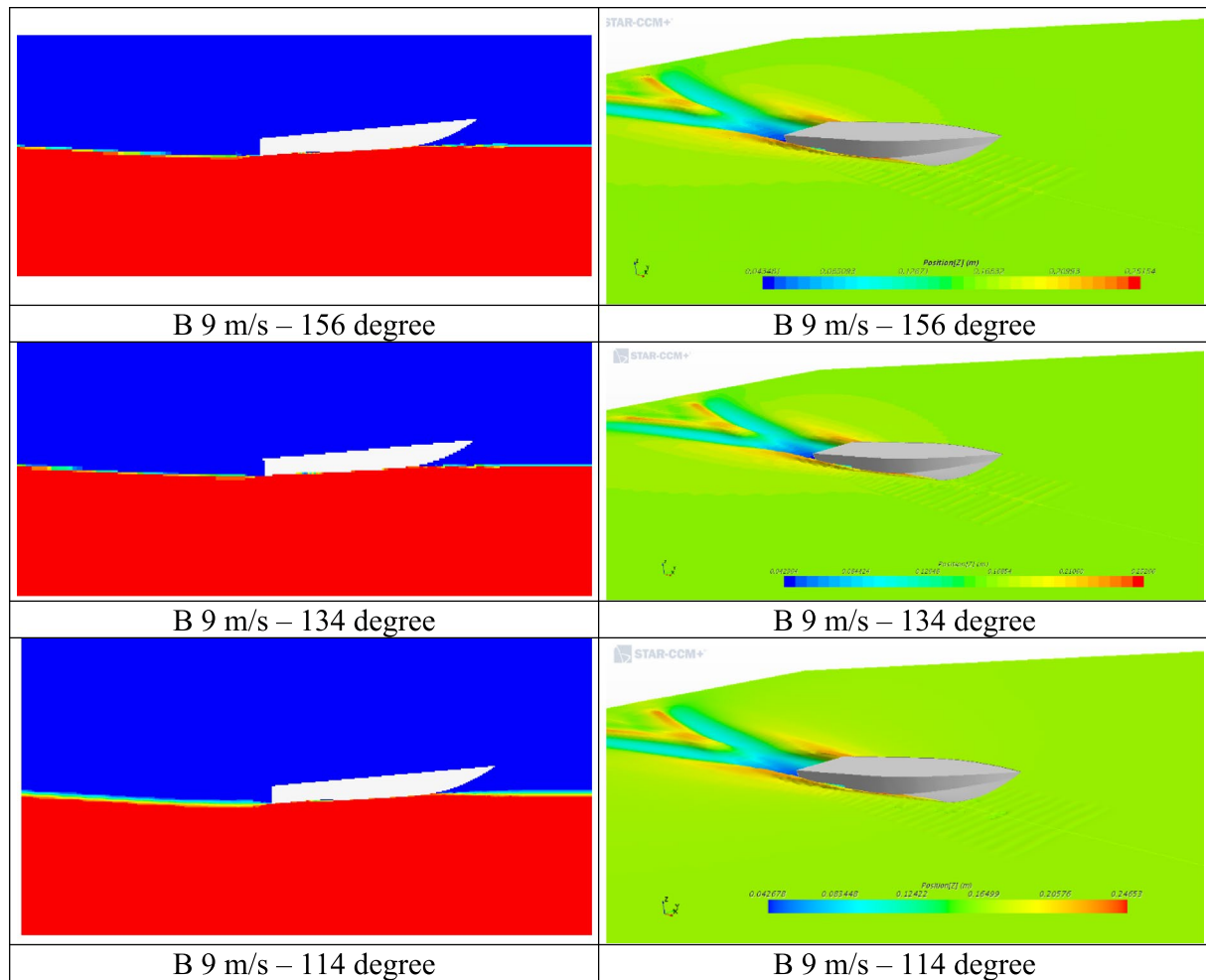
Fig. 18 Wave pattern and rooster tail behind the models equipped with pointed aft step at the speed of 9 m/s and at three different angles of 156, 134, and 114

Declarations

References

Afriantoni A, Romadhoni R, Santoso B (2020) Study on the stability of high speed craft with step hull angle variations. In: The 8th international and national seminar on fisheries and marine science

Brizzolara, S, Federici A (2010) CFD modeling of planning hulls with partially ventilated bottom. In: The William Froude conference: advances in theoretical and applied hydrodynamics—past and future, Portsmouth, pp 24–25

Brizzolara S, Federici A (2013) Designing of planing hulls with longitudinal steps: CFD in support of traditional semi-empirical methods. In: Proceedings of design and construction of super and mega yachts, Genoa, Italy

CD-Adapco (2017). User guide STAR-CCM+ Version 13.0.6

Cucinotta F, Guglielmino E, Sfravara F (2017) An experimental comparison between different artificial air cavity designs for a planing hull. Ocean Eng 140:233–243

De Marco A, Mancini S, Miranda S, Scognamiglio R, Vitiello L (2017) Experimental and numerical hydrodynamic analysis of a stepped planing hull. Appl Ocean Res 64:135–154

Doustdar MM, Kazemi H (2019) Effects of fixed and dynamic mesh methods on simulation of stepped planing craft. J Ocean Eng Sci 4:33–48

Sheingart Z (2014) Hydrodynamics of high speed planing hulls with partially ventilated bottom and hydrofoils. Massachusetts Institute of Technology

Fu TC, Brucker KA, Mousaviraad SM, Ikeda CM, Lee E (2014) An assessment of computational fluid dynamics predictions of the hydrodynamics of high-speed planing craft in calm water and waves. In: 30th Symposium on naval hydrodynamics

Garland W, Maki K (2012) A numerical study of a two-dimensional stepped planing surface. J Ship Prod Des 28(2):60–72

Ghadimi P, Panahi S (2019) Numerical investigation of hydrodynamic forces acting on the non-stepped and double-stepped

planing hulls during yawed steady motion. Proc Inst Mech Eng M J Eng Marit Environ 233(2):428–442

Ghadimi P, Tavakoli S, Dashtimanesh A, Pirooz A (2014) Developing a computer program for detailed study of planing hull's spray based on Morabito's approach. J Mar Sci Appl 13:402–415

Ghadimi P, Panahi S, Tavakoli S (2018) Hydrodynamic study of a double-stepped planing craft through numerical simulations. J Braz Soc Mech Sci Eng 41:1–15

Hay A, Leroyer A, Visonneau M (2006) H-adaptive Navier–Stokes simulations of free-surface flows around moving bodies. J Mar Sci Technol 11:1–18

ITTC (2008a) Testing and extrapolation methods high speed marine vehicles. In: Specialist committee on powering performance prediction 25th ITTC. 75-02-05-01

ITTC (2008b) Uncertainty analysis in CFD verification a validation 7.5-03-01-01, vol 2

ITTC (2011) Recommended Procedures and Guidelines Practical Guidelines for Ship CFD Applications 7.5–03–02–03.

Kazemi H, Salari M (2017) Effects of loading conditions on hydrodynamics of a hard-chine planing vessel using CFD and a dynamic model. Int J Marit Technol 7:11–18

Konstantin I, Matveev M, Ghazi S (2015) Effect of deadrise angles on hydrodynamic performance of a stepped hull. J Eng Marit Environ 230(4):616–622

Lee E, Pavkov M, Mccue W (2014) The systematic variation of step configuration and displacement for a double-step planning craft. J Ship Prod Des 30(2):89–97

Lotfi P, Ashrafizaadeh M, Kowsari Esfahan R (2015) Numerical Investigation of a Stepped Planing Hull in Calm Water. Ocean Eng 94:103–110

Makasyeyev MV (2009) Numerical modeling of cavity flows on bottom of a stepped planing hull. In: Proceedings of the 7th International Symposium on Cavitation. Michigan, USA. Paper No. 116.

Mancini S (2015) The problem of verification and validation processes of CFD simulations of planing hulls. Department of Industrial Engineering, University of Naples Federico II, P.le V. Tecchio n. 80, 80125 Napoli

Matveev KI (2012) Two-dimensional modeling of stepped planing hulls with open and pressurized air cavities. Int J Nav Archit Ocean Eng 4(2):162–171

Niazmand Bilandi R, Mancini S, Vitiello L, Miranda S, De Carlini M (2018) A validation of symmetric 2D + T model based on single-stepped planing hull towing tank tests. J Mar Sci Eng 6(4):136–151

Roache PJ (2002) Code verification by the method of manufactured solutions. J Fluids Eng 124(1):4–10

Sajedi SM, Ghadimi P, Sheikholeslami M, Ghassemi MA (2019) Experimental and numerical analyses of wedge effects on the rooster tail and porpoising phenomenon of a high-speed planing craft in calm water. Proc Inst Mech Eng C J Mech Eng Sci 233(13):4637–4652

Savitsky D, Morabito M (2010) Surface wave contours associated with the forebode wake of stepped planing hulls. Mar Technol 47(1):1–16

Shademani R, Ghadimi P (2017a) Numerical assessment of turbulence effects on forces, spray parameters, and secondary impact in wedge water entry problem using k-epsilon method. Sci Iran 24:223–236

Shademani R, Ghadimi P (2017b) Asymmetric water entry of twin wedges with different deadrises, heel angles, and wedge separations using finite element based finite volume method and VOF. J Appl Fluid Mech 10(1):353–368

Shademani R, Ghadimi P (2017c) Estimation of water entry forces, spray parameters and secondary impact of fixed width wedges at extreme angles using finite element based finite volume and volume of fluid methods. J Fluids Struct 67(1):101–124

Shademani R, Ghadimi P (2017d) Parametric investigation of the effects of deadrise angle and demi-hull separation on impact forces and spray characteristics of catamaran water entry. J Braz Soc Mech Sci Eng 39(6):1989–1999

Svahn D (2009) Performance prediction of hulls with transverse steps. MSc Thesis, KTH, Stockholm

Taunton D, Hudson D, Shenoi R (2010) Characteristics of a series of high-speed hard chine planing hulls-part 1: performance in calm water. J Small Craft Technol 152:55–75

Timmins C (2014) Yaw stability of a recreational stepped planing hull. In: Proceedings of second international Euro conference on high performance marine vehicles, Hamburg, pp 148–158

Vitiello L, Miranda S, Balsamo F, Bove A, Caldarella S (2012) Stepped hulls: model experimental tests and sea trial data. In: Proceedings of the 17th international conference on ships and shipping research, Athena, Greek

Wilson RV, Stern F, Coleman HW, Paterson EG (2001) Comprehensive approach to verification and validation of CFD simulations – part 2: application for RANS simulation of a Cargo/Container ship. J Fluids Eng 123:803–810